

# Hypersharpener by Joint-Criterion Nonnegative Matrix Factorization

Moussa Sofiane Karoui, *Member, IEEE*, Yannick Deville, *Member, IEEE*, Fatima  
Zohra Benhalouche, *Student Member, IEEE*, and Issam Boukerch

Moussa Sofiane Karoui and Fatima Zohra Benhalouche are with the Centre des Techniques Spatiales, 31200 Arzew, Algeria, and with the Institut de Recherche en Astrophysique et Planétologie (IRAP), Université de Toulouse, UPS-OMP, CNRS, 31400 Toulouse, France, and also with the Université des Sciences et de la Technologie d'Oran, 31000 Oran, Algeria (e-mails: {Sofiane.Karoui, Fatima.Benhalouche}@irap.omp.eu).

Yannick Deville is with the Institut de Recherche en Astrophysique et Planétologie (IRAP), Université de Toulouse, UPS-OMP, CNRS, 31400 Toulouse, France (e-mail: Yannick.Deville@irap.omp.eu).

Issam Boukerch is with the Centre des Techniques Spatiales, 31200 Arzew, Algeria (e-mail: issam.boukerch@yahoo.fr).

This work was partly funded by the French ANR project on “HYperspectral imagery for Environmental urban Planning” (HYEP, no. ANR 14-CE22-0016-01), as from Jan. 2015.

## *Abstract*

Hypersharpener aims at combining an observable low spatial resolution hyperspectral image with a high spatial resolution remote sensing image, in particular a multispectral one, to generate an unobservable image with the high spectral resolution of the former and the high spatial resolution of the latter. In this paper, two such new fusion methods are proposed. These methods, related to linear spectral unmixing (LSU) techniques, and based on nonnegative matrix factorization (NMF), optimize a new joint criterion and extend the recently proposed joint nonnegative matrix factorization (JNMF) method. The first approach, called Grd-JCNMF, is a gradient-based method. The second one, called Mult-JCNMF, uses new designed multiplicative update rules. These two joint-criterion nonnegative matrix factorization (JCNMF) approaches are applied to synthetic and semi-real data, and their effectiveness, in spatial and spectral domains, is evaluated with commonly used performance criteria. Experimental results show that the proposed JCNMF methods yield sharpened hyperspectral data with good spectral and spatial fidelities. The obtained results are compared to the performance of two NMF-based methods and one approach based on a sparse representation. These results show that the proposed methods significantly outperform the well-known coupled nonnegative matrix factorization (CNMF) sharpening method for most performance figures. Also, the proposed Mult-JCNMF method provides results that are similar to those obtained by JNMF, with a lower computational cost. Compared with the tested sparse-representation-based approach, the proposed methods give better results. Moreover, the proposed Grd-JCNMF method considerably surpasses all other tested methods.

***Index Terms***

Hyper/multispectral imaging

Data fusion

Hypersharpening

Pansharpening

Linear spectral unmixing

Nonnegative matrix factorization

Author's pre-print version

## I. INTRODUCTION

In optical remote sensing hyperspectral imaging, the sensors collect hundreds or thousands of spectral channels in the visible and infrared wavelength regions (0.4-2.5  $\mu\text{m}$ ). Hyperspectral sensors have a high spectral resolution which allows accurate detection and identification of materials present in the observed scene, but their spatial resolution is often lower than that of multispectral sensors with a low spectral resolution.

Several sharpening methods were designed to merge multispectral or hyperspectral data with a high spatial resolution panchromatic image [1]-[10]. These processes are referred to as pansharpening, and can be grouped in four classes: Component Projection-Substitution (CPS), MultiResolution Analysis (MRA), Bayesian and variational methods. It should here be noted that hybridization between methods of these four classes is possible. Also, it is natural to expect that performing pansharpening with hyperspectral data is more complex than performing it with multispectral data [1]. The pansharpening approaches were extended, in the last decades, in order to fuse hyperspectral and multispectral remote sensing images. The fusion of the latter two types of images differs from the traditional pansharpening process since high-resolution spatial information is not contained only in one spectral band (i.e., panchromatic image), but in multiple spectral bands (i.e., multispectral image). Therefore, a lot of pansharpening methods are inapplicable to fuse hyperspectral and multispectral remote sensing images.

The methods for fusing hyperspectral and multispectral data, referred to as hypersharpening in [2], are a new way to enhance the spatial resolution of hyperspectral data. These methods aim at merging the spectral information from hyperspectral data with spatial information obtained from high spatial resolution

multispectral/hyperspectral data. The resulting estimated unobservable sharpened hyperspectral data allow one performing accurate identification and classification of an observed area at a finer spatial resolution.

Recently, a few methods have been proposed to achieve the hypersharpening process of hyperspectral data [2], [11]-[16]. Other methods [17]-[21], using Linear Spectral Unmixing (LSU) techniques [22], and based on Nonnegative Matrix Factorization (NMF) [23]-[25], were proposed in order to enhance the spatial resolution of hyperspectral data by using a multispectral image. LSU techniques, which correspond to the typical Blind Source Separation (BSS) problem [26], [27], consist in linearly unmixing remote sensing data into a collection of endmember spectra and their corresponding abundance fractions. NMF aims at decomposing a nonnegative matrix into a product of two nonnegative matrices. In [19], [20], the NMF-based hypersharpening method called Coupled Nonnegative Matrix Factorization (CNMF) yields hyperspectral endmember spectra and high spatial resolution abundance fraction maps, by alternately unmixing high-spectral/low-spatial resolution hyperspectral and low-spectral/high-spatial resolution multispectral data by means of NMF. The CNMF method is time-consuming for it uses an alternate NMF-unmixing process involving a whole series of NMF steps every time it switches between the adaptation of the multispectral and hyperspectral variables. In [18], the proposed Joint NMF (JNMF) method simultaneously unmixes hyperspectral and multispectral data by using an NMF technique. The JNMF method is faster than CNMF and yields similar accuracies. This method includes, in addition to the traditional multiplicative update rules of Lee and Seung's method [24], [25], two supplementary update rules involving down/upsampled versions (by using the  $k$ -nearest-neighbors interpolation) of high and low spatial resolution abundance fraction maps. These additional rules, which do not stem directly

from the used criterion, force the high and low spatial resolution abundance fraction maps to be updated in a consistent manner. However, these rules do not necessarily guarantee that the optimized criterion decreases from an iteration to another.

In this paper, two Joint-Criterion NMF (JCNMF) methods are proposed for hyperspectral and multispectral data fusion. These methods, related to LSU techniques, are based on NMF. In these proposed methods, the joint update (already used in the JNMF method) of the high and low spatial resolution abundance fraction maps is included in a new extended criterion, and new update rules are proposed. The first proposed method, called Gradient-based JCNMF (Grd-JCNMF), uses a projected gradient descent algorithm with adaptive learning rates, as defined in Algorithm 4 of [28]. In the second proposed method, called Multiplicative JCNMF (Mult-JCNMF), a multiplicative gradient-based algorithm is proposed. This second algorithm uses new designed multiplicative update rules, which are derived from the first proposed algorithm by expressing the learning rates as functions of the manipulated hyperspectral and multispectral variables. The update rules of the proposed gradient-based method ensure the decrease of the new considered criterion from an iteration to another.

The remainder of this paper is structured as follows. Section 2 describes the mathematical linear mixing model generally used in the LSU techniques and the associated constraints. In Section 3, the proposed methods are presented. Section 4 consists of test results with synthetic and semi-real data. In that section, results obtained by the proposed methods are compared with those obtained by the CNMF and JNMF methods. These results are also compared with those obtained by the tested sparse-representation approach (denoted SR in the following) [13]. Finally, Section 5 concludes this paper.

## II. MATHEMATICAL DATA MODEL

The aim of hyperspectral data sharpening is to generate unobservable high-spatial/high-spectral resolution hyperspectral data  $\tilde{X}_f \in R_+^{N_h \times K_m}$  from observable low-spatial/high-spectral resolution hyperspectral data  $X_h \in R_+^{N_h \times K_h}$  and high-spatial/low-spectral resolution multispectral data  $X_m \in R_+^{N_m \times K_m}$ .  $N_h$  and  $N_m$  are, respectively, the numbers of spectral bands of the hyperspectral and multispectral images.  $K_h$  and  $K_m$  are, respectively, the numbers of pixels of the hyperspectral and multispectral images. Each row vector of the above matrices contains one spectral band. The observable hyper/multispectral images are assumed to be geometrically coregistered and radiometrically corrected.

The observed low-spatial/high-spectral resolution hyperspectral data can be viewed as a linearly-spatially degraded version of unobservable high-spatial/high-spectral resolution hyperspectral data. Therefore,  $X_h$  is such that

$$X_h \approx \tilde{X}_f D, \quad (1)$$

where  $D \in R_+^{K_m \times K_h}$  is a linear operator performing the spatial degradation [29], which is largely used in the image super-resolution field. Ideally, this operator represents the point spread function (also known as the spatial response) of the hyperspectral sensor. This operator can be viewed as a blurring-decimation matrix, which is a block-diagonal sparse matrix having Gaussian filter values [4], [30], [31], or values equal to  $K_h/K_m$  in the simplest case (i.e., when considering a box filter). This matrix is used in a compact form due to its large size. Also, this matrix is used with Gaussian filter values in the conducted experiments.

As explained in Section 1, the methods proposed hereafter are related to LSU techniques, in which each spectral vector associated with a pixel in a remote sensing image is assumed to be a linear mixture of the endmember spectra within the pixel [22].

The above observable matrices are then modeled as [32]

$$X_h \approx \tilde{A}_h \tilde{S}_h, \quad (2)$$

$$X_m \approx \tilde{A}_m \tilde{S}_m. \quad (3)$$

Here, the column vectors of the nonnegative estimated matrices  $\tilde{A}_h \in R_+^{N_h \times L}$  and  $\tilde{A}_m \in R_+^{N_m \times L}$  respectively represent estimated hyperspectral and multispectral endmember spectra, and  $L$  is the number of endmembers. The row vectors of the nonnegative estimated matrices  $\tilde{S}_h \in R_+^{L \times K_h}$  and  $\tilde{S}_m \in R_+^{L \times K_m}$  respectively represent low spatial-resolution and high spatial-resolution abundance fraction maps. These abundance fractions are subject to the well-known abundance sum-to-one constraint: the sum of all entries of any column vector of the estimated matrices  $\tilde{S}_h$  and  $\tilde{S}_m$  is equal to one.

### III. PROPOSED METHODS

The proposed JCNMF methods first jointly unmix  $X_h$  and  $X_m$  by using extended NMF to estimate the set  $\tilde{A}_h$  of hyperspectral endmember spectra and the set  $\tilde{S}_m$  of high-spatial resolution abundance fraction maps. The unobservable sharpened high-spatial resolution hyperspectral image  $\tilde{X}_f$  is then derived by multiplying these two matrices

$$\tilde{X}_f = \tilde{A}_h \tilde{S}_m. \quad (4)$$

The proposed iterative JCNMF algorithms are inspired from the standard NMF methods, which use multiplicative [24], [25] or projected gradient [28] update rules to achieve the NMF-unmixing process. These proposed iterative algorithms consist in optimizing the following extended criterion

$$J = \frac{\alpha}{2} \|X_h - \tilde{A}_h \tilde{S}_h\|_F^2 + \frac{\beta}{2} \|X_m - \tilde{A}_m \tilde{S}_m\|_F^2 + \frac{\gamma}{2} \|\tilde{S}_h - \tilde{S}_m\|_F^2, \quad (5)$$

where  $\|\cdot\|_F$  denotes the Frobenius norm,  $\alpha$ ,  $\beta$  and  $\gamma$  are balancing coefficients, equal to the

inverse of the number of elements of  $X_h$ ,  $X_m$  or  $\tilde{S}_h$  in each Frobenius norm. Since each norm contains a different number of elements, these coefficients are considered in order to avoid optimizing a term with more emphasis than for the others. The matrix  $\tilde{S}_{dm}$  represents the linearly-spatially degraded version of the matrix  $\tilde{S}_m$  as in (1). This degraded matrix can be expressed as

$$\tilde{S}_{dm} = \tilde{S}_m D. \quad (6)$$

Therefore, the considered criterion to be optimized becomes

$$J = \frac{\alpha}{2} \|X_h - \tilde{A}_h \tilde{S}_h\|_F^2 + \frac{\beta}{2} \|X_m - \tilde{A}_m \tilde{S}_m\|_F^2 + \frac{\gamma}{2} \|\tilde{S}_h - \tilde{S}_m D\|_F^2. \quad (7)$$

Note here that in the expression (5) of  $J$ , the optimized variables are:  $\tilde{A}_h$ ,  $\tilde{S}_h$ ,  $\tilde{A}_m$ ,  $\tilde{S}_m$  and  $\tilde{S}_{dm}$ , while in the final expression (7) of  $J$ , the variables are:  $\tilde{A}_h$ ,  $\tilde{S}_h$ ,  $\tilde{A}_m$ , and  $\tilde{S}_m$ . Also, the third term of the considered criterion (5) or (7) can be regarded as a spatial regularization term. This spatial regularization is appropriate since the scale factor between the spatial resolutions of the two images is limited (usually between 2 and 4), while the scale factor between the two spectral resolutions is much higher. Due to the latter factor, the proposed criterion (5) or (7) does not contain a spectral regularization term. Using such a spectral regularization is ideally preferable [5], [33].

The proposed methods are gradient-based methods. Therefore, the criterion (7) is written as follows

$$\begin{aligned} J = & \frac{\alpha}{2} \text{Tr}(X_h X_h^T - X_h \tilde{S}_h^T \tilde{A}_h^T - \tilde{A}_h \tilde{S}_h X_h^T + \tilde{A}_h \tilde{S}_h \tilde{S}_h^T \tilde{A}_h^T) \\ & + \frac{\beta}{2} \text{Tr}(X_m X_m^T - X_m \tilde{S}_m^T \tilde{A}_m^T - \tilde{A}_m \tilde{S}_m X_m^T + \tilde{A}_m \tilde{S}_m \tilde{S}_m^T \tilde{A}_m^T) \\ & + \frac{\gamma}{2} \text{Tr}(\tilde{S}_h \tilde{S}_h^T - \tilde{S}_h D^T \tilde{S}_m^T - \tilde{S}_m D \tilde{S}_h^T + \tilde{S}_m D D^T \tilde{S}_m^T), \end{aligned} \quad (8)$$

where  $\text{Tr}(\cdot)$  and  $(\cdot)^T$  respectively denote the matrix trace and the matrix transpose. This formulation of the criterion easily permits one to derive the gradient expressions, using the properties in [34]:

$$\frac{\partial J}{\partial \tilde{A}_h} = \alpha(\tilde{A}_h \tilde{S}_h \tilde{S}_h^T - X_h \tilde{S}_h^T), \quad (9)$$

$$\frac{\partial J}{\partial \tilde{S}_h} = \alpha(\tilde{A}_h^T \tilde{A}_h \tilde{S}_h - \tilde{A}_h^T X_h) + \gamma(\tilde{S}_h - \tilde{S}_m D), \quad (10)$$

$$\frac{\partial J}{\partial \tilde{A}_m} = \beta(\tilde{A}_m \tilde{S}_m \tilde{S}_m^T - X_m \tilde{S}_m^T), \quad (11)$$

$$\frac{\partial J}{\partial \tilde{S}_m} = \beta(\tilde{A}_m^T \tilde{A}_m \tilde{S}_m - \tilde{A}_m^T X_m) + \gamma(\tilde{S}_m D D^T - \tilde{S}_h D^T). \quad (12)$$

For the first proposed method (Grd-JCNMF), and applying the gradient descent algorithm, the following update rules are obtained:

$$\tilde{A}_h \leftarrow \tilde{A}_h - \varphi_{\tilde{A}_h} \frac{\partial J}{\partial \tilde{A}_h}, \quad (13)$$

$$\tilde{S}_h \leftarrow \tilde{S}_h - \varphi_{\tilde{S}_h} \frac{\partial J}{\partial \tilde{S}_h}, \quad (14)$$

$$\tilde{A}_m \leftarrow \tilde{A}_m - \varphi_{\tilde{A}_m} \frac{\partial J}{\partial \tilde{A}_m}, \quad (15)$$

$$\tilde{S}_m \leftarrow \tilde{S}_m - \varphi_{\tilde{S}_m} \frac{\partial J}{\partial \tilde{S}_m}, \quad (16)$$

where  $\varphi_{\tilde{A}_h}$ ,  $\varphi_{\tilde{S}_h}$ ,  $\varphi_{\tilde{A}_m}$  and  $\varphi_{\tilde{S}_m}$  are small positive and adaptive learning rates, calculated by using the ‘‘Armijo rule along the projection arc’’ as defined in Algorithm 4 of [28]. Applying these update rules is not sufficient because they do not guarantee nonnegativity. To ensure the nonnegativity constraint, each element of the updated matrix is compared with a very small positive value  $\varepsilon$  (generally set to the default MATLAB *epsilon* value), and the maximum between them is kept [23]. Therefore, the final iterative update rules for the first proposed method are

$$\tilde{A}_h \leftarrow \max \{ \tilde{A}_h - \varphi_{\tilde{A}_h} \frac{\partial J}{\partial \tilde{A}_h}, \varepsilon \}, \quad (17)$$

$$\tilde{S}_h \leftarrow \max \{ \tilde{S}_h - \varphi_{\tilde{S}_h} \frac{\partial J}{\partial \tilde{S}_h}, \varepsilon \}, \quad (18)$$

$$\tilde{A}_m \leftarrow \max \{ \tilde{A}_m - \varphi_{\tilde{A}_m} \frac{\partial J}{\partial \tilde{A}_m}, \varepsilon \}, \quad (19)$$

$$\tilde{S}_m \leftarrow \max \{ \tilde{S}_m - \varphi_{\tilde{S}_m} \frac{\partial J}{\partial \tilde{S}_m}, \varepsilon \}. \quad (20)$$

For the second proposed method (Mult-JCNMF), multiplicative update rules are derived from the above gradient-based update rules. These multiplicative update rules are obtained by expressing the learning rates  $\varphi$  as functions of the considered matrices. Each expression of a learning rate is chosen so as to yield a multiplicative update and to preserve the nonnegativity. The first point (i.e., the multiplicativity) is guaranteed if the learning rate contains the term of the considered updated matrix in its numerator, to permit an element-wise factorization of this updated matrix. To fulfill the second point (i.e., the nonnegativity), all terms, in the gradient expressions (9)-(12), preceded by a plus sign must be removed from (13)-(16) to obtain a sum of positive terms in (13)-(16). This is achieved by placing those terms in the denominator of the considered learning rate, which will permit the elimination of these terms when reducing the whole expression in the right-hand side of (13)-(16) to the same denominator [35]. Based on this principle, the learning rates become the following matrices

$$\varphi_{\tilde{A}_h} = \tilde{A}_h \oslash (\alpha \tilde{A}_h \tilde{S}_h \tilde{S}_h^T), \quad (21)$$

$$\varphi_{\tilde{S}_h} = \tilde{S}_h \oslash (\alpha \tilde{A}_h^T \tilde{A}_h \tilde{S}_h + \gamma \tilde{S}_h), \quad (22)$$

$$\varphi_{\tilde{A}_m} = \tilde{A}_m \oslash (\beta \tilde{A}_m \tilde{S}_m \tilde{S}_m^T), \quad (23)$$

$$\varphi_{\tilde{S}_m} = \tilde{S}_m \oslash (\beta \tilde{A}_m^T \tilde{A}_m \tilde{S}_m + \gamma \tilde{S}_m D D^T), \quad (24)$$

where  $\oslash$  corresponds to element-wise division. Therefore, the final iterative multiplicative update rules for the second proposed method are

$$\tilde{A}_h \leftarrow \tilde{A}_h \odot ((X_h S_h^T) \oslash (\tilde{A}_h \tilde{S}_h \tilde{S}_h^T + \epsilon)), \quad (25)$$

$$\tilde{S}_h \leftarrow \tilde{S}_h \odot ((\alpha \tilde{A}_h^T X_h + \gamma \tilde{S}_m D) \oslash (\alpha \tilde{A}_h^T \tilde{A}_h \tilde{S}_h + \gamma \tilde{S}_h + \epsilon)), \quad (26)$$

$$\tilde{A}_m \leftarrow \tilde{A}_m \odot ((X_m S_m^T) \oslash (\tilde{A}_m \tilde{S}_m \tilde{S}_m^T + \epsilon)), \quad (27)$$

$$\tilde{S}_m \leftarrow \tilde{S}_m \odot ((\beta \tilde{A}_m^T X_m + \gamma \tilde{S}_h D^T) \oslash (\beta \tilde{A}_m^T \tilde{A}_m \tilde{S}_m + \gamma \tilde{S}_m D D^T + \epsilon)), \quad (28)$$

where  $\odot$  corresponds to element-wise multiplication, and  $\epsilon$  (very small and positive value: again generally set to the default MATLAB *epsilon* value) is added to the

denominator of each multiplicative update rule to avoid possible division by zero.

The proposed JCNMF methods, as standard NMF methods, have limitations, i.e. they are not guaranteed to provide a unique solution and their convergence point may depend on their initialization. Indeed, a key issue of these algorithms is how to initialize them. To solve this problem, and to avoid random initialization from the point of view of the proposed JCNMF algorithms, and as the initialization phase, the initial estimated hyperspectral endmember spectra  $\tilde{A}_h^{(0)}$  are calculated by the Vertex Component Analysis (VCA) method [36], which is one of the famous used methods in LSU techniques. The VCA method requires the number  $L$  of endmembers to be known. This number is automatically detected in our approaches by using the Hyperspectral Signal Subspace Identification by Minimum Error (HySime) method [37]. The initial estimated low-spatial resolution abundance fraction maps  $\tilde{S}_h^{(0)}$  are derived from the low-spatial/high-spectral resolution observed hyperspectral image  $X_h$  and the initial estimated matrix  $\tilde{A}_h^{(0)}$ , by means of the Fully Constrained Least Squares (FCLS) method [38], separately applied to each pixel of the hyperspectral image. The initial estimated multispectral endmember spectra  $\tilde{A}_m^{(0)}$  are derived from the initial estimated hyperspectral spectra  $\tilde{A}_h^{(0)}$  by simply averaging the samples of the latter spectra over the wavelength regions used in the multispectral image. The initial estimated high-spatial resolution abundance fraction maps  $\tilde{S}_m^{(0)}$  are derived from the high-spatial/low-spectral resolution observed multispectral image  $X_m$  and the initial estimated matrix  $\tilde{A}_m^{(0)}$ , by means of the FCLS method, again separately applied to each pixel of the multispectral image. Note here that this dependent initialization of hyperspectral and multispectral variables allows avoiding a possible permutation of the endmembers between the results of the two used hyper/multispectral images unmixing processes. Such a permutation

would be problem when using fusion equation (4). Also, the known problem related to the scale factor that can appear in the results of the two unmixing processes, and that is also a problem when using fusion equation (4), is avoided by the sum-to-one constraint imposed on high/low spatial resolution abundance fraction maps.

After initializing all the considered hyper/multispectral matrices as described above, the optimization phase consists in jointly and repeatedly updating these matrices, until convergence (defined hereafter), according to (17)-(20) for the Grd-JCNMF method or (25)-(28) for the Mult-JCNMF method. It should here be noted that the designed update rules (17)-(20) or (25)-(28) yield a decreasing criterion  $J$  during this optimization stage, in practice. Also and to satisfy the abundance sum-to-one constraint throughout this stage, the method described in [38] is adopted. The convergence criterion is defined by checking if the relative modification of criterion  $J$  takes a value below a given threshold  $tresh$ , i.e.

$$\left| \frac{J^{(t)} - J^{(t+1)}}{J^{(t)}} \right| \leq tresh. \quad (29)$$

Also, and to avoid a high number of iterations, an additional stopping criterion is obtained by also checking if this number of iterations exceeds a predefined maximum.

The whole algorithms derived from the proposed methods are described below.

---

**Algorithm 1:** Grd-JCNMF unmixing for sharpening hyperspectral data.

---

**Input:** low-spatial/high-spectral resolution hyperspectral image  $X_h$  and high-spatial/low-spectral resolution multispectral image  $X_m$ .

---

1- Calculate the blurring-decimation matrix  $D$  with Gaussian filter values [29].

2- Estimate the number  $L$  of endmembers by using the HySime Method.

3- **Initialization stage**

3.1- Initialize  $\tilde{A}_h$  from  $X_h$  by using the VCA method.

3.2- Initialize  $\tilde{S}_h$  from  $X_h$  and initial  $\tilde{A}_h$  by using the FCLS method.

3.3- Initialize  $\tilde{A}_m$  from initial  $\tilde{A}_h$ .

3.4- Initialize  $\tilde{S}_m$  from  $X_m$  and initial  $\tilde{A}_m$  by using the FCLS method.

4- **Optimization stage** (for each iteration and until convergence)

4.1- Optimize  $\tilde{A}_h$  by using (17).

4.2- Optimize  $\tilde{S}_h$  by using (18).

4.3- Optimize  $\tilde{A}_m$  by using (19).

4.4- Optimize  $\tilde{S}_m$  by using (20).

5- **Fusion stage**

5.1- Fuse  $\tilde{A}_h$  and  $\tilde{S}_m$  by using (4) to get  $\tilde{X}_f$ .

---

**Output:** high-spatial/high-spectral resolution sharpened hyperspectral data  $\tilde{X}_f$ .

---

---

**Algorithm 2:** Mult-JCNMF unmixing for sharpening hyperspectral data.

---

**Input:** low-spatial/high-spectral resolution hyperspectral image  $X_h$  and high-spatial/low-spectral resolution multispectral image  $X_m$ .

---

1- Calculate the blurring-decimation matrix  $D$  with Gaussian filter values [29].

2- Estimate the number  $L$  of endmembers by using the HySime Method.

3- **Initialization stage**

3.1- Initialize  $\tilde{A}_h$  from  $X_h$  by using the VCA method.

3.2- Initialize  $\tilde{S}_h$  from  $X_h$  and initial  $\tilde{A}_h$  by using the FCLS method.

3.3- Initialize  $\tilde{A}_m$  from initial  $\tilde{A}_h$ .

3.4- Initialize  $\tilde{S}_m$  from  $X_m$  and initial  $\tilde{A}_m$  by using the FCLS method.

4- **Optimization stage** (for each iteration and until convergence)

4.1- Optimize  $\tilde{A}_h$  by using (25).

4.2- Optimize  $\tilde{S}_h$  by using (26).

4.3- Optimize  $\tilde{A}_m$  by using (27).

4.4- Optimize  $\tilde{S}_m$  by using (28).

5- **Fusion stage**

5.1- Fuse  $\tilde{A}_h$  and  $\tilde{S}_m$  by using (4) to get  $\tilde{X}_f$ .

---

**Output:** high-spatial/high-spectral resolution sharpened hyperspectral data  $\tilde{X}_f$ .

---

## IV. TEST RESULTS

### A. Tested data

#### A.1. Synthetic data

The tested synthetic data are generated from a real airborne high-spatial/high-spectral resolution hyperspectral image, with 224 spectral bands in the 0.40-2.50  $\mu\text{m}$  region and 3.5 m spatial resolution. This 400x400 pixel real hyperspectral image, acquired by the Airborne Visible/Infrared Imaging Spectrometer (AVIRIS) sensor, is spatially and spectrally degraded to generate synthetic low-spatial/high-spectral resolution hyperspectral and high-spatial/low-spectral resolution multispectral images. These spatial and spectral degradations yield synthetic data with reduced spatial and spectral resolutions for validation exploiting a protocol that may be related to the Wald's one, which was initially developed for the pansharpening processes [3], [6], [39]. The synthetic low-spatial/high-spectral resolution hyperspectral image is obtained, from the real hyperspectral image (used as a reference image), by using a 2x2 pixel Gaussian filter [30], [31] in a 1<sup>st</sup> experiment, and a 4x4 pixel Gaussian filter in a 2<sup>nd</sup> one, which results in a 200x200 pixel image (corresponding to 7 m spatial resolution) in the 1<sup>st</sup> experiment, and a 100x100 pixel image (corresponding to 14 m spatial resolution) in the 2<sup>nd</sup> experiment. The synthetic high-spatial/low-spectral resolution multispectral image is derived from the real hyperspectral image by averaging the spectral band values which cover different wavelength domains. Five scenarios, described in Table I, are considered. Scenarios 1 and 2 use a limited number of multispectral spectral bands, with adjacent bands (scenario 1) or distant bands (scenario 2). The number of multispectral spectral bands increases each time in the following scenarios (i.e. scenarios 3-5). Thus, synthetic multispectral 400x400 pixel images are obtained, with 3.5 m spatial resolution and with 3, 3, 4, 5 and 6 spectral bands respectively in the 1<sup>st</sup> to 5<sup>th</sup> scenarios.

**Table I.** Description of the different scenarios: (a) index of scenario, (b) number of wavelength domains.

(a)	(b)	Wavelength domains ( $\mu\text{m}$ )
1	3	0.45-0.52, 0.52-0.60, and 0.63-0.69
2	3	0.45-0.52, 0.52-0.60, and 2.08-2.35
3	4	0.45-0.52, 0.52-0.60, 0.63-0.69, and 0.76-0.90
4	5	0.45-0.52, 0.52-0.60, 0.63-0.69, 0.76-0.90, and 1.55-1.75
5	6	0.45-0.52, 0.52-0.60, 0.63-0.69, 0.76-0.90, 1.55-1.75, and 2.08-2.35

### A.2. Semi-real data

In these investigations, unlike in [11]-[14], [17], [19], semi-real data are used. These semi-real data (geometrically coregistered and radiometrically corrected), acquired on the same day (March 3, 2003) and at the same time, cover a part of Oran urban area, Algeria. The residual spatial misalignments, between these semi-real data, are lower than a pixel (maximum absolute value), which can be acceptable due to the different acquisition geometries of the considered sensors [40]. The hyperspectral image is from the Earth Observing-1 (EO-1) Hyperion sensor. This image, with 30 m spatial resolution, contains 125 spectral bands after removing, from the original 242 spectral band data cube, the low signal to noise ratio spectral bands as well as the non-calibrated and overlapping spectral bands. Two pansharpened versions (by using the Gram-Schmidt (GS) method [3]) of multispectral images are used. The first one, acquired by the Landsat Enhanced Thematic Mapper plus (ETM+) sensor, is characterized by 6 spectral bands and 15 m spatial resolution. The second one, acquired by the EO-1 Advanced Land Imager (ALI) sensor, with 10 m spatial resolution, contains 9 spectral bands.

## ***B. Performance evaluation criteria***

Many quality metrics/protocols were developed for assessing the hypersharpening processes with or without reference [3], [6], [8], [37]-[39], [41]-[43].

For the tested synthetic data, the spectral and spatial qualities of the estimated sharpened hyperspectral image are evaluated by comparing it with the reference hyperspectral image. To evaluate the spectral reconstruction quality, the Spectral Angle Mapper (SAM) [19] criterion is used. This criterion is calculated between each pixel spectrum in the reference image and its analogue in the estimated image. A smaller angle indicates a better spectral reconstruction. In the spatial domain, the used criteria are: the Peak Signal to Noise Ratio (PSNR) [19], the Universal Image Quality Index (UIQI), with values between -1 and 1 [44], and the Relative Dimensionless Global Error in Synthesis (ERGAS: French acronym for “Erreur Relative Globale Adimensionnelle de Synthèse”) [8]. These spatial criteria are calculated between each spectral band in the reference image and its analogue in the estimated one. The highest PSNR, UIQI values correspond to the best spatial reconstruction quality. The ideal ERGAS value is 0.

For the tested semi-real data, a modified Quality with No Reference (mQNR) criterion is proposed and used as a spatial-spectral reconstruction quality index. The standard QNR [42] has been modified to be used in the considered hypersharpening processes.

This modified criterion reads

$$\text{mQNR} = (1 - D_\lambda)^\rho (1 - D_s)^\sigma, \quad (30)$$

where  $\rho$  and  $\sigma$  are real-valued exponents (set to 1 in the conducted experiments).  $D_\lambda$  and  $D_s$  are spectral and spatial distortion indices. The spectral distortion index reads

$$D_\lambda = \sqrt[q]{\frac{1}{N_h(N_h-1)} \sum_{j=1}^{N_h} \sum_{r=1, r \neq j}^{N_h} \left| \text{UIQI}(X_{f_j}, X_{f_r}) - \text{UIQI}(X_{h_j}, X_{h_r}) \right|^q}, \quad (31)$$

where  $q$  is a positive integer exponent (set to 1 in the conducted experiments).  $X_f$  is one

spectral band of the sharpened hyperspectral image.  $X_h$  is one spectral band of the hyperspectral image. The spatial distortion index  $D_s$  is calculated as follows. For each spectral band of the multispectral image, a spatial distortion sub-index is estimated. This sub-index is calculated, by using the standard index defined in [42], between each multispectral spectral band and hyperspectral bands covered by the same multispectral band. The hyperspectral bands outside the spectral range of the multispectral band are not considered. The final spatial distortion index  $D_s$  represents the mean of the calculated sub-indices. Note here that each sub-index uses a spatial downsampling operation. This operation is performed by using the above defined blurring-decimation matrix  $D$  with Gaussian filter values.

The range of mQNR,  $D_\lambda$ , and  $D_s$  is [0, 1]. A higher mQNR value indicates a higher spatial-spectral reconstruction quality. A smaller spectral (respectively spatial) distortion value indicates a better spectral (respectively spatial) reconstruction.

### **C. Results and discussion**

The proposed Grd-JCNMF and Mult-JCNMF methods are applied to the above data sets. The maximum number of iterations used in these proposed methods is set to 10. This number is also considered in the learning rate adaptation loop in the Grd-JCNMF method. The JNMF and CNMF methods are also considered in the performed experiments for comparison purposes. The JNMF method uses a small positive parameter to jointly update (downsampled)-high/(upsampled)-low spatial resolution abundance fraction maps [18]. This parameter is set to 0.1 in the considered experiments. The maximum number of iterations considered in the JNMF method is set to 10. The CNMF method contains two loops: inner and outer loops [19]. In the conducted experiments, the maximum number of iterations of the inner (respectively outer) loop is set to 10 (respectively 3). The threshold value of the convergence criterion

(29) is set to  $10^{-6}$  for all the used methods. The SR-based method [13] is also considered in the conducted experiments.

The CPU used in the conducted experiments is an Intel(R) Core(TM) i5 processor running at 2.50 GHz, with a memory capacity of 4 GB.

In the following tables, the computational costs, the means of the SAM, PSNR, and UIQI criteria, and the ERGAS values, are given for the tested synthetic data in all the considered scenarios for both experiments 1 and 2.

Globally, these tables show that the proposed Grd-JCNMF and Mult-JCNMF approaches yield satisfactory spatial and spectral fidelities for the sharpened hyperspectral images. For both experiments 1 and 2, these tests confirm the overall superiority of the proposed methods as compared with the literature NMF-based approaches. Indeed, Grd-JCNMF provides the overall best fusion accuracies, but its computational costs are its drawback. Mult-JCNMF overcomes this weak point, by yielding the lowest computational costs and overall fusion results that are similar to those obtained by the JNMF method and better than those of CNMF, especially in the first scenario. Moreover, the Grd-JCNMF method considerably surpasses all other tested methods. These tables also show that the proposed methods yield satisfactory results even with a limited number of multispectral spectral bands, with adjacent bands (scenario 1) or distant bands (scenario 2), while the CNMF method gives poor results with few adjacent multispectral spectral bands (scenario 1). Also, these tables show, as expected, that the results generally improve as the number of multispectral spectral bands increases (ignoring the effect of non-adjacent bands in scenario 2).

**Table II.** Computational costs, means of SAM, PSNR, and UIQI criteria, and the ERGAS criterion - Synthetic data (scenario 1).

		Multi-JCNMF	Grd-JCNMF	JNMF	CNMF	SR
Experiment 1	Time (sec)	<b>19.13</b>	244.89	20.28	163.39	6944.08
	SAM (°)	11.43	<b>9.01</b>	13.59	12.62	10.82
	PSNR (dB)	21.61	<b>25.03</b>	23.59	18.87	22.00
	UIQI	0.74	<b>0.84</b>	0.70	0.54	0.63
	ERGAS	21.00	<b>11.43</b>	14.12	27.01	23.16
Experiment 2	Time (sec)	<b>11.08</b>	221.06	13.33	134.23	5704.78
	SAM (°)	8.28	<b>7.83</b>	11.45	12.21	10.47
	PSNR (dB)	23.66	26.43	18.48	23.54	<b>27.45</b>
	UIQI	0.75	<b>0.85</b>	0.49	0.59	0.69
	ERGAS	27.42	<b>24.33</b>	62.01	38.52	33.04

**Table III.** Computational costs, means of SAM, PSNR, and UIQI criteria, and the ERGAS criterion - Synthetic data (scenario 2).

		Multi-JCNMF	Grd-JCNMF	JNMF	CNMF	SR
Experiment 1	Time (sec)	<b>18.94</b>	249.98	20.58	164.34	6984.45
	SAM (°)	9.89	<b>6.32</b>	10.99	11.49	9.85
	PSNR (dB)	23.31	<b>29.87</b>	27.23	23.97	27.95
	UIQI	0.85	<b>0.93</b>	0.86	0.70	0.82
	ERGAS	15.90	<b>9.50</b>	11.73	17.93	15.38
Experiment 2	Time (sec)	<b>11.06</b>	221.05	12.89	136.36	5795.30
	SAM (°)	<b>7.07</b>	7.69	8.74	10.57	9.07
	PSNR (dB)	26.49	30.10	20.62	27.61	<b>32.19</b>
	UIQI	<b>0.89</b>	<b>0.89</b>	0.72	0.86	0.87
	ERGAS	20.23	<b>19.29</b>	44.62	21.42	20.37

**Table IV.** Computational costs, means of SAM, PSNR, and UIQI criteria, and the ERGAS criterion - Synthetic data (scenario 3).

		Multi-JCNMF	Grd-JCNMF	JNMF	CNMF	SR
Experiment 1	Time (sec)	<b>20.42</b>	243.00	22.36	445.13	18918.03
	SAM (°)	15.31	<b>5.18</b>	9.46	19.85	17.02
	PSNR (dB)	20.37	<b>31.44</b>	24.79	24.89	29.02
	UIQI	0.64	<b>0.93</b>	0.85	0.69	0.80
	ERGAS	29.47	<b>10.44</b>	17.19	27.74	23.79
Experiment 2	Time (sec)	<b>14.06</b>	218.77	14.67	139.06	5910.05
	SAM (°)	5.90	<b>5.26</b>	8.65	8.93	7.66
	PSNR (dB)	29.28	<b>31.31</b>	24.97	30.62	30.70
	UIQI	<b>0.94</b>	0.93	0.88	0.90	0.93
	ERGAS	21.55	<b>20.97</b>	32.08	25.96	22.26

**Table V.** Computational costs, means of SAM, PSNR, and UIQI criteria, and the ERGAS criterion - Synthetic data (scenario 4).

		Multi-JCNMF	Grd-JCNMF	JNMF	CNMF	SR
Experiment 1	Time (sec)	<b>23.16</b>	270.30	26.17	479.55	20380.88
	SAM (°)	4.09	3.18	<b>2.92</b>	4.96	4.25
	PSNR (dB)	31.21	37.41	34.77	35.21	<b>41.05</b>
	UIQI	0.96	<b>0.98</b>	<b>0.98</b>	0.97	<b>0.98</b>
	ERGAS	11.27	7.64	7.98	8.88	<b>7.62</b>
Experiment 2	Time (sec)	<b>13.81</b>	221.39	14.03	139.98	5949.15
	SAM (°)	3.54	<b>3.06</b>	3.78	3.21	3.15
	PSNR (dB)	32.50	<b>37.67</b>	32.12	35.83	36.78
	UIQI	0.98	<b>0.99</b>	0.98	0.98	0.98
	ERGAS	17.85	<b>15.02</b>	17.55	16.37	16.01

**Table VI.** Computational costs, means of SAM, PSNR, and UIQI criteria, and the ERGAS criterion - Synthetic data (scenario 5).

		Multi-JCNMF	Grd-JCNMF	JNMF	CNMF	SR
Experiment 1	Time (sec)	<b>21.30</b>	243.39	23.89	458.45	19484.13
	SAM (°)	2.51	<b>2.06</b>	2.79	2.27	2.15
	PSNR (dB)	34.05	<b>40.59</b>	37.43	36.24	40.26
	UIQI	<b>0.99</b>	<b>0.99</b>	<b>0.99</b>	<b>0.99</b>	<b>0.99</b>
	ERGAS	7.74	<b>5.72</b>	6.70	6.87	5.89
Experiment 2	Time (sec)	<b>12.77</b>	219.02	15.08	137.86	5859.05
	SAM (°)	3.17	<b>2.10</b>	2.24	3.35	2.87
	PSNR (dB)	33.64	<b>40.08</b>	38.91	33.42	33.97
	UIQI	<b>0.99</b>	<b>0.99</b>	<b>0.99</b>	0.98	<b>0.99</b>
	ERGAS	15.14	<b>11.85</b>	12.37	15.70	13.46

Also for the synthetic data, and considering the 2<sup>nd</sup> experiment, scenario 5, Fig. 1 to 3 are given as an example. These figures show the spectral bands, respectively, in the 0.815, 1.65 and 2.218  $\mu\text{m}$  regions [17], [19], of the original high spatial resolution hyperspectral image, the low spatial resolution hyperspectral image, and the high spatial resolution hyperspectral images estimated by the proposed Grd-JCNMF and CNMF methods, and the absolute differences between the original and estimated spectral bands. As expected, it is difficult to determine the differences between the original image and both estimated images with visual inspection. Table VII illustrates the basic statistics of the absolute differences between the original and estimated spectral bands. This table shows that the estimated spectral bands, obtained using the proposed method, are significantly closer to the original spectral bands than the spectral bands estimated by the CNMF approach.

**Table VII.** Basic parameters (minimum: min, maximum: max, mean, and standard deviation: std) of the absolute differences between the original and estimated spectral bands - Synthetic data (2<sup>nd</sup> experiment, scenario 5).

Spectral region	parameter	Original - Grd-JCNMF	Original - CNMF
0.815 $\mu\text{m}$	min	<b>0.0000</b>	<b>0.0000</b>
	max	<b>0.0450</b>	0.1551
	mean	<b>0.0015</b>	0.0155
	std	<b>0.0019</b>	0.0140
1.65 $\mu\text{m}$	min	<b>0.0000</b>	<b>0.0000</b>
	max	<b>0.0558</b>	0.1401
	mean	<b>0.0021</b>	0.0103
	std	<b>0.0030</b>	0.0094
2.218 $\mu\text{m}$	min	<b>0.0000</b>	<b>0.0000</b>
	max	<b>0.0597</b>	0.1313
	mean	<b>0.0035</b>	0.0093
	std	<b>0.0033</b>	0.0087

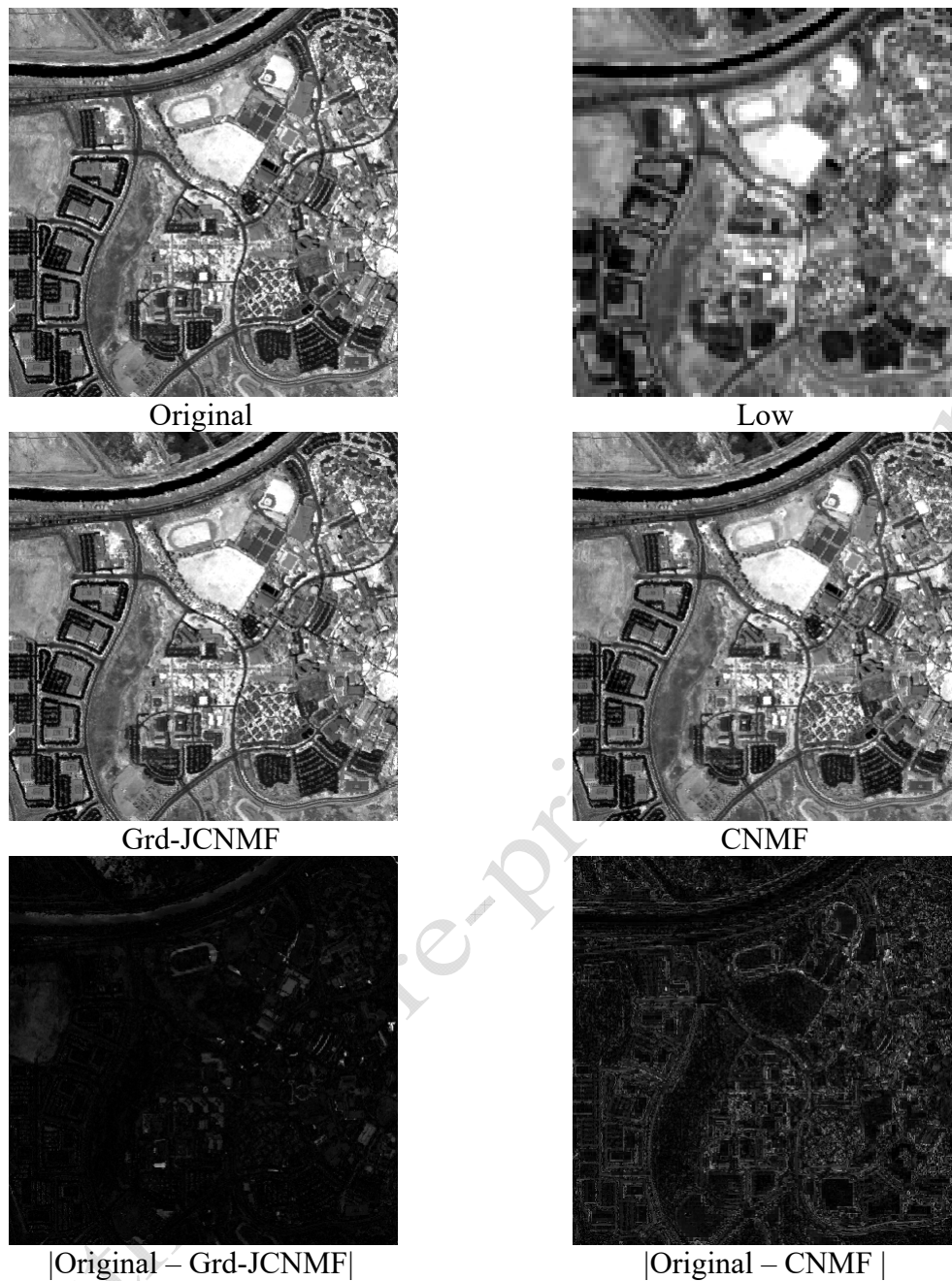


**Fig. 1.** Spectral bands, in the 0.815  $\mu\text{m}$  region, of the original high spatial resolution hyperspectral image, the low spatial resolution hyperspectral image, and the estimated high spatial resolution hyperspectral images, and the absolute differences between the original and estimated spectral bands - Synthetic data, 2<sup>nd</sup> experiment, scenario 5.

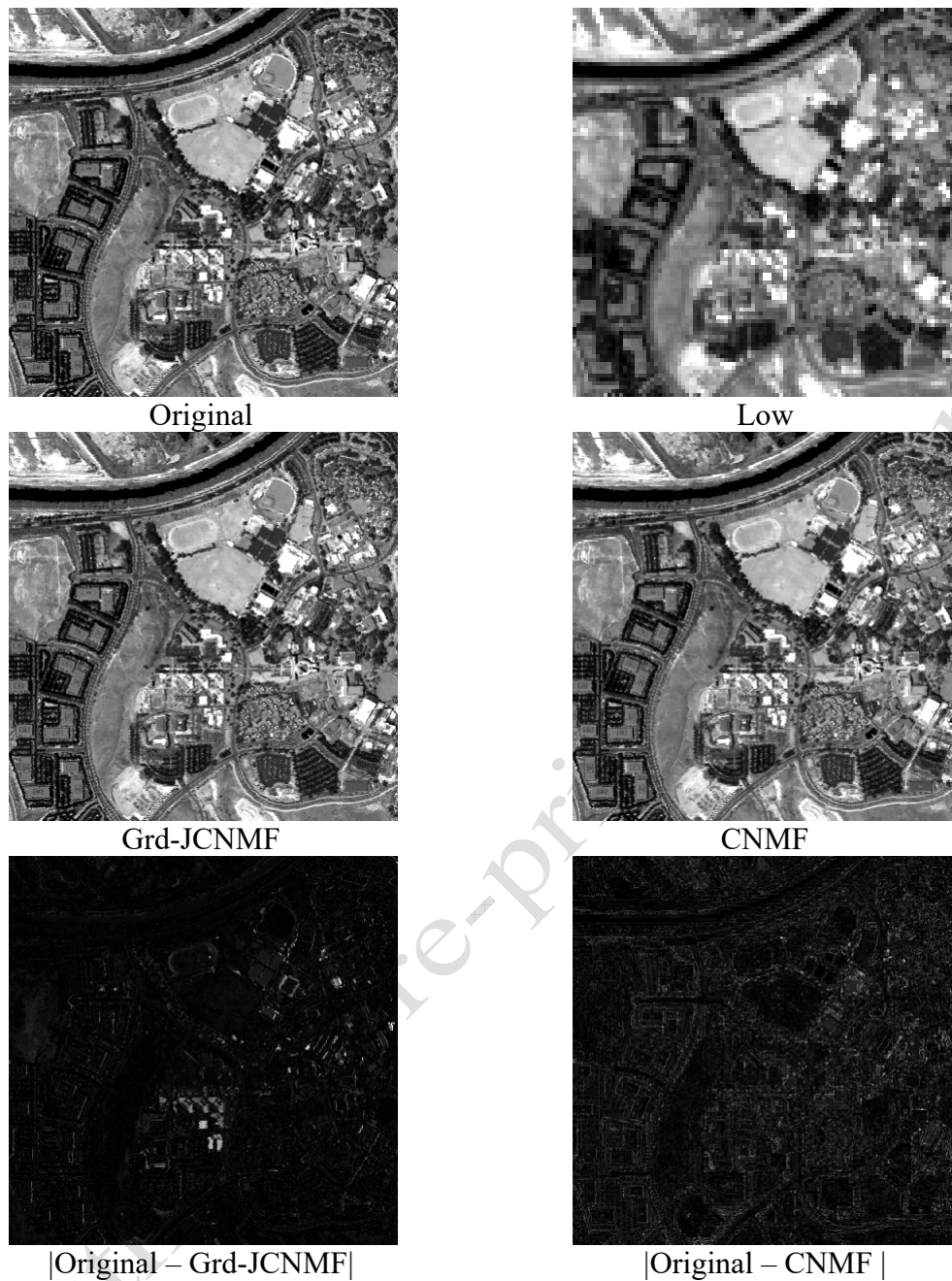


**Fig. 2.** Spectral bands, in the  $1.65 \mu\text{m}$  region, of the original high spatial resolution hyperspectral image, the low spatial resolution hyperspectral image, and the estimated high spatial resolution hyperspectral images, and the absolute differences between the original and estimated spectral bands - Synthetic data, 2<sup>nd</sup> experiment, scenario 5.

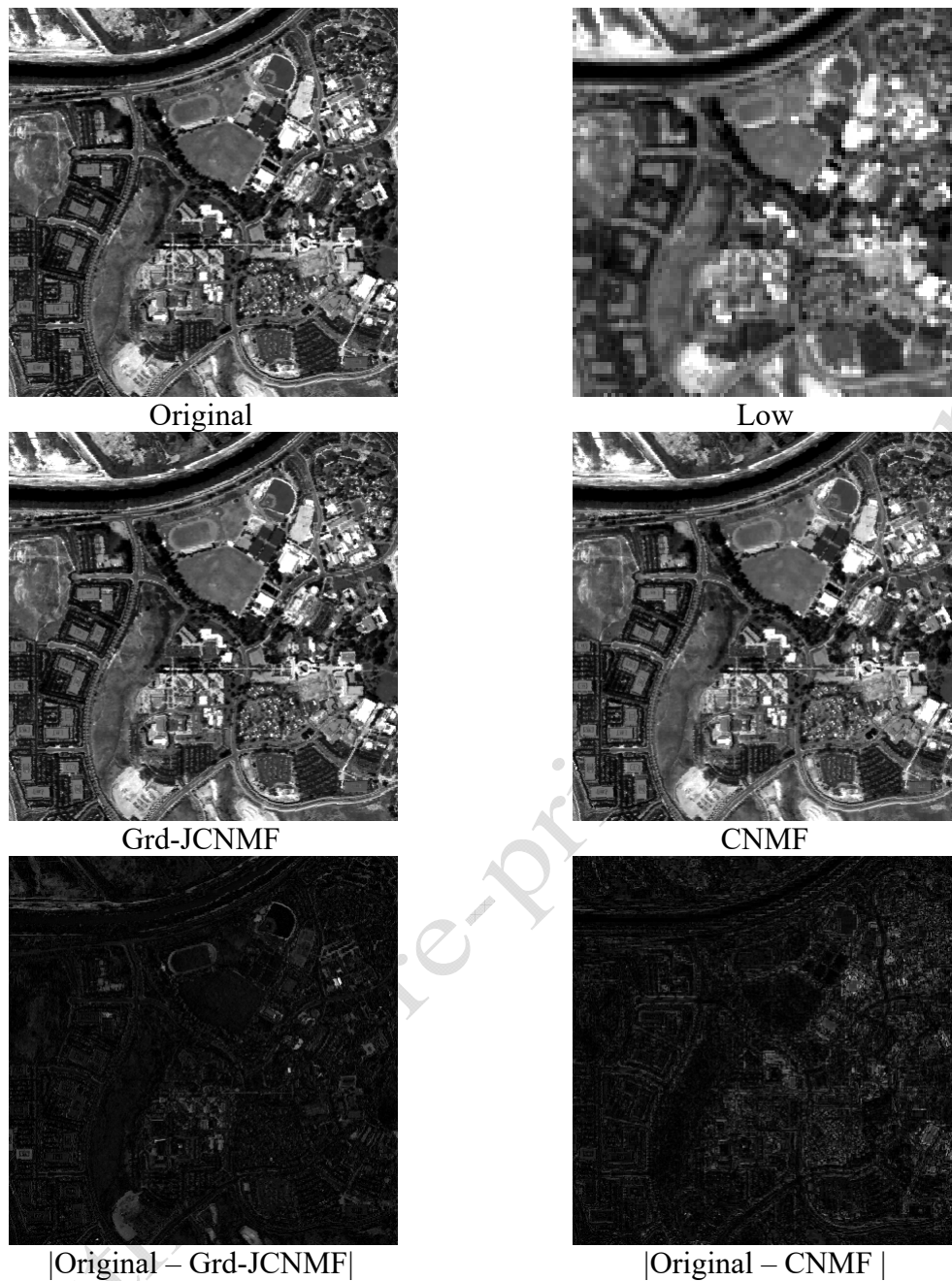


**Fig. 3.** Spectral bands, in the 2.218  $\mu\text{m}$  region, of the original high spatial resolution hyperspectral image, the low spatial resolution hyperspectral image, and the estimated high spatial resolution hyperspectral images, and the absolute differences between the original and estimated spectral bands - Synthetic data, 2<sup>nd</sup> experiment, scenario 5.

For the semi-real data, the results (spatial and spectral distortions and mQNR criteria values) obtained with all tested methods are given in Table VIII. This table also confirms the superiority (in terms of spatial and spectral reconstructions) of the proposed methods as compared with the tested literature methods.

Fig. 4 shows the spectral bands, in the 0.815  $\mu\text{m}$  region, of the low spatial resolution hyperspectral image and the high spatial resolution hyperspectral images estimated by the Grd-JCNMF and CNMF methods.

**Table VIII.** Computational costs, spatial and spectral distortions and mQNR criteria values - Semi-real data.

		Multi-JCNMF	Grd-JCNMF	JNMF	CNMF	SR
EO-1	Time (sec)	<b>10.53</b>	153.66	12.55	79.48	3377.90
Hyperion with Landsat ETM+	$D_s$	<b>0.10</b>	<b>0.10</b>	<b>0.10</b>	0.11	<b>0.10</b>
	$D_\lambda$	0.04	<b>0.02</b>	0.06	0.11	0.09
	mQNR	0.86	<b>0.88</b>	0.84	0.79	0.82
EO-1	Time (sec)	<b>18.55</b>	295.00	20.20	105.22	4471.85
Hyperion with EO-1 ALI	$D_s$	<b>0.17</b>	0.20	0.21	0.21	0.20
	$D_\lambda$	0.06	<b>0.05</b>	0.08	0.10	0.08
	mQNR	<b>0.78</b>	0.76	0.73	0.71	0.74

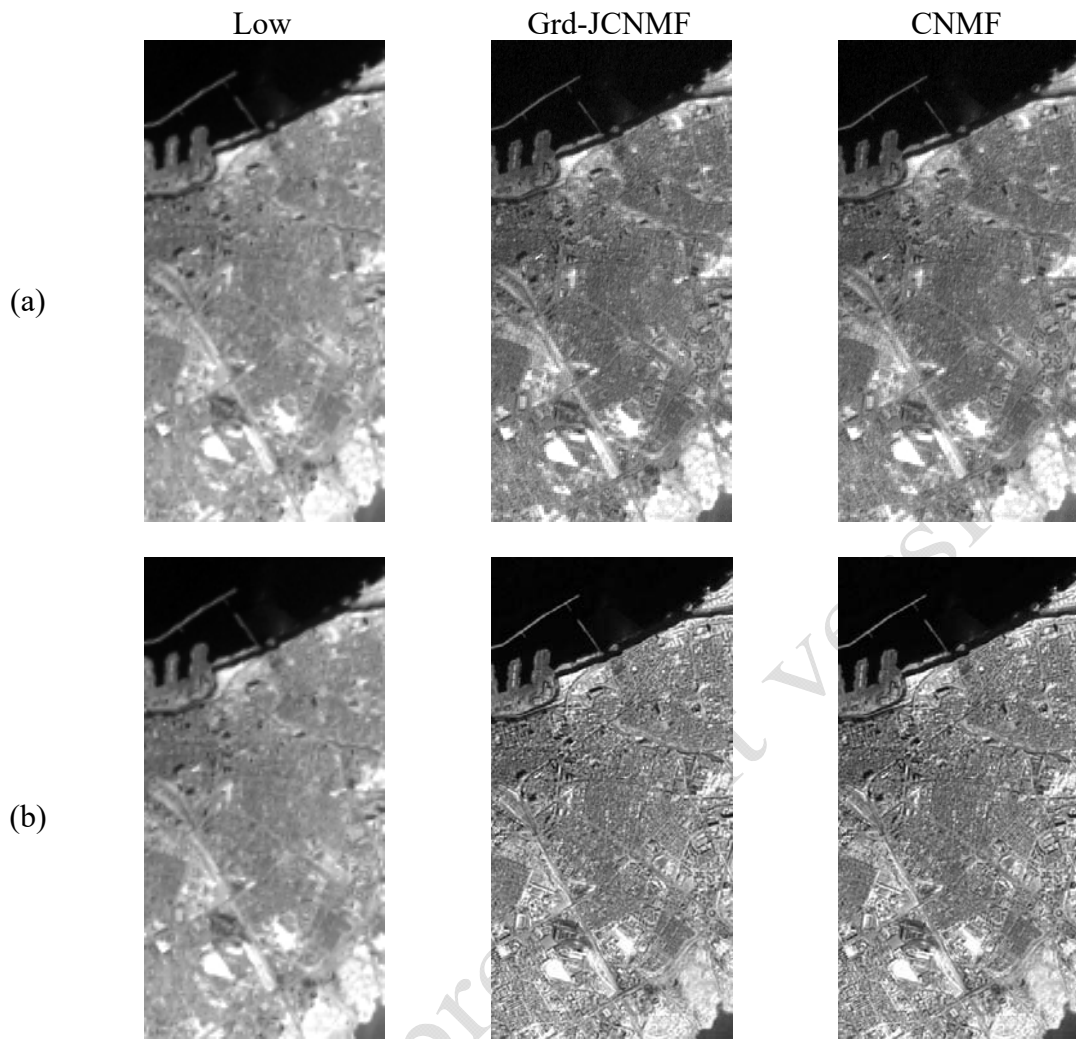


**Fig. 4.** Spectral bands, in the  $0.815 \mu\text{m}$  region, of the low spatial resolution hyperspectral image and the high spatial resolution hyperspectral images estimated by the Grd-JCNMF and CNMF methods: (a) EO-1 Hyperion with Landsat ETM+, (b) EO-1 Hyperion with EO-1 ALI.

It should here be noted that the given computational costs (for all conducted experiments) are merely indicative, and are not used as comparison criteria. These computational costs are given only to allow the readers to have an idea about the execution time of each used method. Indeed, using the computational costs, it is difficult to compare differently constructed methods (with different criteria to be optimized and different numbers of used loops). In addition, the computational costs

provided above are obtained when the used methods stop after reaching the maximum number of iterations and not the satisfaction of the convergence criterion (29).

Finally, the differences in the results obtained with the two proposed Mult-JCNMF and Grd-JCNMF methods can also be explained by the different numbers of used loops in each method.

## V. CONCLUSION

In this paper, two methods, called Grd-JCNMF and Mult-JCNMF, were proposed for fusing low-spatial/high-spectral resolution hyperspectral and high-spatial/low-spectral resolution multispectral images. These methods, related to LSU techniques, are based on NMF. The proposed methods optimize a new criterion which permits joint update of hyper/multispectral variables. The first method uses a projected gradient descent algorithm with adaptive learning rates. In the second method, a multiplicative gradient-based algorithm was proposed.

The proposed approaches were applied to synthetic and semi-real data, and their effectiveness, in spatial and spectral domains, were evaluated with commonly used performance criteria. Experimental results show that the proposed methods yield sharpened hyperspectral data with good spectral and spatial fidelities. These new methods significantly outperform the CNMF method from the literature for most performance figures. Compared with the tested sparse representation approach, the proposed methods give better results. The proposed Grd-JCNMF approach provides the best fusion accuracies, but its computational costs are its drawback. The Mult-JCNMF method overcomes this weak point, by giving the lowest computational costs and fusion results that are similar to those obtained by the JNMF method.

The proposed methods are easy to implement, and the high qualities of the sharpened JCNMF data in both spatial and spectral domains can undoubtedly contribute to the accurate identification and classification of an observed area at a finer spatial resolution.

*Author's pre-print version*

## **ACKNOWLEDGEMENT**

The authors would like to thank the developers of the used literature algorithms for sharing their MATLAB implementations. The authors would also like to take this opportunity to gratefully thank the Associate Editor and the Anonymous Reviewers for their outstanding comments and suggestions that greatly improved the technical quality and presentation of this manuscript.

*Author's pre-print version*

## REFERENCES

- [1] L. Loncan, L. B. Almeida, J. M. Bioucas-Dias, X. Briottet, J. Chanussot, N. Dobigeon, S. Fabre, W. Liao, G. A. Licciardi, M. Simões, J.-Y. Tourneret, M. A. Veganzones, G. Vivone, Q. Wei, and N. Yokoya, "Hyperspectral pansharpening: a review," *IEEE Geoscience and Remote Sensing Magazine*, 3(3), pp. 27-46, 2015.
- [2] M. Selva, B. Aiazzi, F. Butera, L. Chiarantini, and S. Baronti, "Hyper-sharpening: A first approach on SIM-GA data," *IEEE Journal of Selected Topics in Applied Earth Observations and Remote Sensing*, vol. 8(6), pp. 3008-3024, 2015.
- [3] G. Vivone, L. Alparone, J. Chanussot, M. Dalla Mura, A. Garzelli, G. Licciardi, R. Restaino, and L. Wald, "A Critical Comparison Among Pansharpening Algorithms," *IEEE Transactions on Geoscience and Remote Sensing*, vol. 53(5), pp. 2565-2586, 2015.
- [4] G. Vivone, M. Simoes, M. Dalla Mura, R. Restaino, J. M. Bioucas-Dias, G. Licciardi, and J. Chanussot, "Pansharpening Based on Semiblind Deconvolution," *IEEE Transactions on Geoscience and Remote Sensing*, vol. 53(4), pp. 1997-2010, 2015.
- [5] C. Thomas, T. Ranchin, L. Wald, and J. Chanussot, "Synthesis of Multispectral Images to High Spatial Resolution: A Critical Review of Fusion Methods Based On Remote Sensing Physics," *IEEE Transactions on Geoscience and Remote Sensing*, 46(5), pp. 1301-1312, 2008.
- [6] L. Alparone, L. Wald, J. Chanussot, C. Thomas, P. Gamba, and L. M. Bruce, "Comparison of pansharpening algorithms: Outcome of the 2006 GRS-S data fusion contest," *IEEE Transactions on Geoscience and Remote Sensing*, vol. 45(10), pp. 3012-3021, 2007.

- [7] B. Aiazzi, L. Alparone, S. Baronti, and A. Garzelli, "Context-driven fusion of high spatial and spectral resolution images based on oversampled multiresolution analysis," *IEEE Transactions on Geoscience and Remote Sensing*, vol. 40(10), pp. 2300-2312, 2002.
- [8] L. Wald, *Data Fusion: Definitions and Architectures - Fusion of Images of Different Spatial Resolutions*, Les Presses de l'École des Mines, Paris, France, 2002.
- [9] C. Laben and B. Brower, "Process for enhancing the spatial resolution of multispectral imagery using pan-sharpening," *U.S. Patent 6 011 875*, 2000.
- [10] P. S. Chavez Jr., S. C. Sides, and J. A. Anderson, "Comparison of three different methods to merge multiresolution and multispectral data: Landsat TM and SPOT panchromatic," *Photogrammetric Engineering & Remote Sensing*, vol. 57(3), pp. 295-303, 1991.
- [11] F. Palsson, J. R. Sveinsson, M. O. Ulfarson, and J. A. Benediktsson, "Model-Based Fusion of Multi- and Hyperspectral Images Using PCA and Wavelets," *IEEE Transactions on Geoscience and Remote Sensing*, 53(5), pp. 2652-2663, 2015.
- [12] Q. Wei, N. Dobigeon, and J.-Y. Tourneret, "Bayesian Fusion of Hyperspectral and Multispectral Images," in *Proc. IEEE ICASSP*, pp. 3176-3180, 2014.
- [13] Q. Wei, J. M. Bioucas-Dias, N. Dobigeon, and J.-Y. Tourneret, "Hyperspectral and Multispectral Images Fusion Based on a Sparse Representation," *IEEE Transactions on Geoscience and Remote Sensing*, 53(7), pp. 3658-3668, 2015.
- [14] Q. Wei, N. Dobigeon, and J.-Y. Tourneret, "Fast Fusion of Multi-Band Images Based on Solving a Sylvester Equation," *IEEE Transactions on Image Processing*, 24(11), pp. 4109-4121, 2015.

- [15] M. T. Eismann, R. C. Hardie, "Hyperspectral resolution enhancement using high-resolution multispectral imagery with arbitrary response functions," *IEEE Transactions on Geoscience and Remote Sensing*, vol. 43(3), pp. 455-465, 2005.
- [16] R. B. Gomez, A. Jazaeri, and M. Kafatos, "Wavelet-based hyperspectral and multispectral image fusion," in *Proc. SPIE*, vol. 4383, pp. 36-42, 2001.
- [17] M. A. Bendoumi, M. He, and S. Mei, "Hyperspectral Image Resolution Enhancement Using High-Resolution Multispectral Image Based on Spectral Unmixing," *IEEE Transactions on Geoscience and Remote Sensing*, 52(10), pp. 6574-6583, 2014.
- [18] M. S. Karoui, Y. Deville, and S. Kreri, "Joint Nonnegative Matrix Factorization for Hyperspectral and Multispectral Remote Sensing Data Fusion," in *Proc. IEEE WHISPERS*, 2013.
- [19] N. Yokoya, T. Yairi, and A. Iwasaki, "Coupled Nonnegative Matrix Factorization Unmixing for Hyperspectral and Multispectral Data Fusion," *IEEE Transactions on Geoscience and Remote Sensing*, 50(2), pp. 528-537, 2012.
- [20] O. Berné, A. Tielens, P. Pilleri, and C. Joblin, "Non-negative matrix factorization pansharpening of hyperspectral data: An application to mid-infrared astronomy," in *Proc. IEEE WHISPERS*, 2010.
- [21] J. Bieniarz, D. Cerra, J. Avbelj, P. Reinartz, and R. Müller, "Hyperspectral image resolution enhancement based on spectral unmixing and information fusion," *Int. Arch. Photogramm. Remote Sens. Spatial Inf. Sci.*, XXXVIII-4/W19, pp. 33-37, 2011.
- [22] J. M. Bioucas-Dias, A. Plaza, N. Dobigeon, M. Parente, Q. Du, P. Gader, and J. Chanussot, "Hyperspectral Unmixing Overview: Geometrical, Statistical, and Sparse Regression-Based Approaches," *IEEE Journal of Selected Topics in Applied Earth Observations and Remote Sensing*, vol. 5(2), pp. 354-379, 2012.

- [23] A. Cichocki, R. Zdunek, A. H. Phan, and S. I. Amari, *Nonnegative Matrix and Tensor Factorizations: Applications to Exploratory Multi-way Data Analysis and Blind Source Separation*, John Wiley & Sons, Chichester, UK, 2009.
- [24] D. D. Lee, H. S. Seung, "Learning the parts of objects by non-negative matrix factorization," *Nature (401)*, pp. 788-791, 1999.
- [25] D. D. Lee, H. S. Seung, "Algorithms for Non-Negative Matrix Factorization," *Advances in Neural Information Processing Systems, 13*, pp. 556-562, MIT Press, 2001.
- [26] P. Comon, C. Jutten, *Handbook of Blind Source Separation: Independent Component Analysis and Applications*, Academic Press, Oxford, UK, 2010.
- [27] Y. Deville, *Blind Source Separation and Blind Mixture Identification Methods*, Wiley Encyclopedia of Electrical and Electronics Engineering, pp. 1-33, 2016.
- [28] C.-J. Lin, "Projected Gradient Methods for Non-negative Matrix Factorization," *Neural Computation, 19(10)*, pp. 2756-2779, 2007.
- [29] P. P. Gajjar, M. V. Joshi, A. Banerjee, and S. Mitra, "Decimation Estimation and Linear-Based Super-Resolution Using Zoomed Observations," *Pattern Recognition and Image Analysis, Lecture Notes in Computer Science, 4477*, pp. 314-321, 2007.
- [30] P. Massip, P. Blanc, and L. Wald, "A method to better account for modulation transfer functions in arsis-based pansharpening methods," *IEEE Transactions on Geoscience and Remote Sensing, vol. 50(3)*, pp. 800-808, 2012.
- [31] B. Aiazzi, L. Alparone, S. Baronti, A. Garzelli, and M. Selva, "MTF-tailored multiscale fusion of high-resolution MS and Pan imagery," *Photogrammetric Engineering & Remote Sensing, vol. 72(5)*, pp. 591-596, 2006.
- [32] M. S. Karoui, Y. Deville, S. Hosseini, and A. Ouamri, "Blind spatial unmixing of multispectral images: New methods combining sparse component analysis, clustering and non-negativity constraints," *Pattern Recognition, 45(12)*, pp. 4263-4278, 2012.

- [33] H. R. Shahdoosti and H. Ghassemian, "Fusion of MS and PAN Images Preserving Spectral Quality," *IEEE Geoscience and Remote Sensing Letters*, vol. 12(3), pp. 611-615, 2015.
- [34] K. B. Petersen, M. S. Pedersen, *The matrix Cookbook*, Technical Univ. Denmark, 2008 [Online]. Available: URL:<http://matrixcook-book.com/>
- [35] I. Meganem, Y. Deville, S. Hosseini, P. Déliot, and X. Briottet, "Linear-Quadratic Blind Source Separation Using NMF to Unmix Urban Hyperspectral Images," *IEEE Transactions on Signal Processing*, 62(7), pp. 1822-1833, 2014.
- [36] J. M. P. Nascimento, J. M. Bioucas-Dias, "Vertex Component Analysis: A Fast Algorithm to Unmix Hyperspectral Data," *IEEE Transactions on Geoscience and Remote Sensing*, 43(4), pp. 898-910, 2005.
- [37] J. M. Bioucas-Dias, J. M. P. Nascimento, "Hyperspectral subspace identification," *IEEE Transactions on Geoscience and Remote Sensing*, vol. 46(8), pp. 2435-2445, 2008.
- [38] D.C. Heinz, C.I. Chang, "Fully constrained least squares linear spectral mixture analysis method for material quantification in hyperspectral imagery," *IEEE Transactions on Geoscience and Remote Sensing*, vol. 39(3), pp. 529-545, 2001.
- [39] L. Wald, T. Ranchin, and M. Mangolini, "Fusion of satellite images of different spatial resolutions: Assessing the quality of resulting images," *Photogrammetric Engineering & Remote Sensing*, vol. 63(6), pp. 691-699, 1997.
- [40] B. Aiazzi, S. Baronti, M. Selva, L. Alparone, "Bi-cubic interpolation for shift-free pan-sharpening," *ISPRS Journal of Photogrammetry and Remote Sensing*, vol. 86, pp. 65-76, 2013.

- [41] L. Alparone, S. Baronti, A. Garzelli, and F. Nencini, "A Global Quality Measurement of Pan-sharpened Multispectral Imagery," *IEEE Geoscience and Remote Sensing Letters*, vol. 1(4), pp. 313-317, 2004.
- [42] L. Alparone, B. Aiazzi, S. Baronti, A. Garzelli, F. Nencini, and M. Selva, "Multispectral and Panchromatic Data Fusion Assessment Without Reference," *Photogrammetric Engineering & Remote Sensing*, vol. 74(2), pp. 193-200, 2008.
- [43] A. Garzelli and F. Nencini, "Hypercomplex Quality Assessment of Multi/Hyperspectral Images," *IEEE Geoscience and Remote Sensing Letters*, vol. 6(4), pp. 662-665, 2009.
- [44] Z. Wang, A. C. Bovik, "A Universal Image Quality Index," *IEEE Signal Processing Letters*, 9(3), pp. 81-84, 2002.



Moussa Sofiane Karoui was born in Oran, Algeria, in 1979. In 2000, he graduated in Applied Mathematics from the Université Es-Sénia, Oran, Algeria. In 2007, he received his M.Sc. degree in Signal and Image Processing from the Université Paul Sabatier Toulouse 3, Toulouse, France. In 2008, he received his Magister's degree in Signal and Image Processing from the Université des Sciences et de la Technologie, Oran, Algeria. In 2012, he received his Ph.D. degree in Signal and Image Processing from the Université Paul Sabatier Toulouse 3, Toulouse, France, co-supervised with the Université des Sciences et de la Technologie, Oran, Algérie. Since 2001, he is a Senior Researcher at the Centre des Techniques Spatiales, Arzew, Algeria. His current major activities include linear/nonlinear spectral/spatial unmixing techniques in remote sensing imagery, statistical and especially, BSS methods with applications to remote sensing imagery.



Yannick Deville was born in Lyon, France, in 1964. He graduated from the Ecole Nationale Supérieure des Télécommunications de Bretagne (Brest, France) in 1986. He received his D.E.A. and Ph.D. degrees, both in Microelectronics, from the University of Grenoble (France), in 1986 and 1989, respectively. From 1986 to 1997, he was a Research Scientist at Philips Research Labs (Limeil, France). His investigations during this period concerned various fields, including GaAs integrated microwave RC active filters, VLSI cache memory architectures and replacement algorithms, neural network algorithms and applications, and nonlinear systems. Since 1997, he has been a Professor at the University of Toulouse (France). From 1997 to 2004, he was with the Acoustics lab of that University. Since 2004, he has been with the Astrophysics lab in Toulouse,

which is part of the University but also of the French National Center for Scientific Research (CNRS) and of the Midi-Pyrénées Observatory. His current major research interests include signal and image processing (especially hyperspectral data), higher-order statistics, time–frequency analysis, neural networks, and especially Blind Source Separation and Independent Component Analysis methods and their applications to Remote Sensing, Astrophysics and Quantum Information Processing.



Fatima Zohra Benhalouche was born in Oran, Algeria, in 1989. She received the M.Sc. degree in Signal and Image Processing from the Université des Sciences et de la Technologie, Oran, Algeria in 2012. Currently, she is working towards the Ph.D. degree at Université

Paul Sabatier Toulouse 3, Toulouse, France, co-supervised with the Université des Sciences et de la Technologie, Oran, Algeria. Since 2016, she is a Junior Researcher at the Centre des Techniques Spatiales, Arzew, Algeria. Her main research interests concern unmixing and fusion of multispectral and hyperspectral remote sensing data.



Issam Boukerch was born in Tipaza, Algeria, in 1979. In 2003, he graduated in Geodetic Sciences and Surveying from the Centre National des Techniques Spatiales, Arzew, Algeria. In 2006, he received his M.Sc. degree in Space Sciences and Technologies from

the Centre Regional Africain des Sciences et des Technologies de l’Espace en Langue Française, Rabat, Morocco. Currently, he is working towards the Ph.D. degree at the Université d’Oran 2, Oran, Algeria. Since 2003, he is a Senior Researcher at the Centre des Techniques Spatiales, Arzew, Algeria. His main research interests concern close range photogrammetry and geometric modeling of remote sensing imagery systems.